



HAL
open science

PhysOM: Physarum polycephalum Oriented Microstructures

David-henri Garnier, Martin-Pierre Schmidt, Damien Rohmer

► **To cite this version:**

David-henri Garnier, Martin-Pierre Schmidt, Damien Rohmer. PhysOM: Physarum polycephalum Oriented Microstructures. Computer Graphics Forum, 2024, 10.1111/cgf.15075 . hal-04572077v2

HAL Id: hal-04572077


<https://hal.science/hal-04572077v2>

Submitted on 15 May 2024

HAL is a multi-disciplinary open access archive for the deposit and dissemination of scientific research documents, whether they are published or not. The documents may come from teaching and research institutions in France or abroad, or from public or private research centers.

L'archive ouverte pluridisciplinaire **HAL**, est destinée au dépôt et à la diffusion de documents scientifiques de niveau recherche, publiés ou non, émanant des établissements d'enseignement et de recherche français ou étrangers, des laboratoires publics ou privés.

PhysOM: *Physarum polycephalum* Oriented Microstructures

D. H. Garnier¹ , M. P. Schmidt² and D. Rohmer¹ 

¹ LIX, Ecole Polytechnique, CNRS, IP Paris, France

² LMI, Normandie Univ., INSA Rouen, 76000 Rouen, France

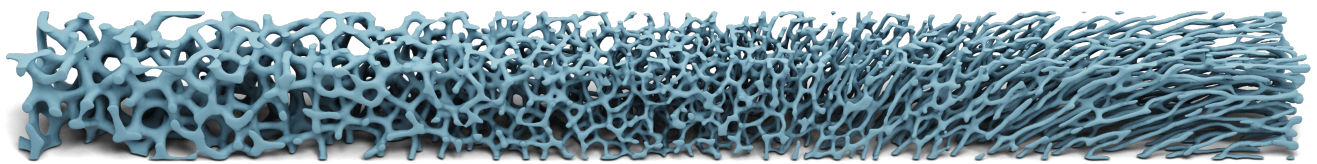


Figure 1: Our parameterized 3D anisotropic *Physarum polycephalum* model is able to generate foam-like cells and filaments ranging from coarse to dense cells (left side), to varying orientation and elongation magnitude (right side).

Abstract

*Biological shapes possess fascinating properties and behaviors that are the result of emergent mechanisms: they can evolve over time, dynamically adapt to changes in their environment, while also exhibiting interesting mechanical properties and aesthetic appeal. In this work, we bring and extend an existing biological-inspired model of the *Physarum polycephalum*, aka the blob, to the field of computer graphics, in order to design porous organic-like microstructures that resemble natural foam-like cells or filament-like patterns with variable local properties. In contrast to approaches based on static global optimization that provides only limited expressivity over the result, our method allows precise control over the local orientation of 3D patterns, relative cell extension, and precise infill of shapes with well defined boundaries. To this end, we extend the classical agent-based model for *Physarum* to fill an arbitrary domain with local anisotropic behavior. We further provide a detailed analysis of the model parameters, contributing to the understanding of the system behavior. The method is fast, parallelizable and scalable to large volumes, and compatible with user interaction, allowing a designer to guide the structure, erase parts, and observe its evolution in real-time. Overall, our method provides a versatile and efficient means of generating intricate organic microstructures that have potential applications in fields such as additive manufacturing, design, or biological representation and engineering.*

CCS Concepts

• *Computing methodologies* → *Shape modeling*;

1. Introduction

Microstructure-made synthetic materials, which refer to small-scale structures filling the interior domain of a larger shape, have become increasingly popular in shape design. These materials offer desirable mechanical properties, including local stiffness, lightness, and porosity [WWG21], that can be tailored by varying the type of infill patterns. Furthermore, these microstructures exhibit visually compelling appearances, mimicking complex organic materials that may interest art-based design [MSDL17]. In this work, we focus on microstructure exhibiting foam-looking patterns made of oriented foam-like cells, or long filament organizations (see Fig. 1) and relate their parameters to mechanical and visually appealing characteristics.

In recent years, the study of complex shapes filled with mi-

crostructures has gained significant attention due to the efficiency of additive manufacturing to build them, in particular along the so-called topological optimization methods. However, designing these materials still presents several challenges. Firstly, creating intricate and delicate micro-structures that occupy relatively large volumes can result in laborious modeling, massive data structures, and prohibitively high computational costs associated with global optimization. Secondly, microstructure shapes can be highly diverse, which adds significant complexity to the design process and requires meticulous tailoring and parameterization for each object to achieve the expected behavior and appearance.

Through this work, we wish to highlight the power of adapted bioinspired morphogenesis approach to tackle such challenges. Indeed, real biological systems have evolved to optimize their struc-

29 tures and functions through a variety of mechanisms, including
30 self-assembly, growth, and adaptation. Morphogenesis models in-
31 spired by biological systems typically rely on local rules from
32 which global characteristics emerge from an iterative process, pos-
33 sibly representing time evolution. A key interest of such a local
34 and time-evolving process relies upon its inherent adaptation to lo-
35 cal conditions and its ability to generate organic-like microstruc-
36 tures that follow a general pattern while exhibiting irregular local
37 variations. One may note that disordered porous structures found
38 in nature are neither fully random nor perfectly ordered. Inter-
39 estingly this structural disorder in organic architected cellular
40 materials has been found to be beneficial for their damage toler-
41 ance [vEYC*21]. These remarks led to our main motivation for
42 exploring biological-inspired microstructure generation. Instead of
43 aiming at a globally optimized shape model that would be hard to
44 control, we rather target locally adaptable behaviors that can give
45 rise to a global emerging structure, which remains controllable by
46 the end user at any time of the evolution, and provide a visual ap-
47 pealing organic-looking disorder that enhances strength.

48 In this work, we show that the biological system designated as
49 *Physarum polycephalum*, also known as *the blob* [How31] can be
50 adapted to model our target microstructure for 3D shapes in a con-
51 trollable way. This slime mold is a unicellular organism that has
52 gained attention in recent years as it has been found to exhibit re-
53 markable capabilities for optimizing transport networks, and adapt-
54 ing to changing environments. The *Physarum polycephalum* can
55 be represented by an agent-based models [Jon09] simulating vari-
56 ous aspects of the organism behavior including its growth, forag-
57 ing, and decision-making processes. Existing simulations of this
58 model already showed the natural emergence of global structures in
59 2D [Jon10] and in 3D [Jon15, EBPF20a, EBPF22] but were never
60 explored for oriented microstructures generation. We describe sev-
61 eral adaptations and/or simplifications to the existing models to ex-
62 tend it to oriented organic-foam-looking emerging microstructure,
63 and provide insights into the choice of the model and simulation
64 parameters to converge toward the expected shape characteristics
65 effectively. Our technical contributions are twofolds. First, we ex-
66 tend the existing agent-based physarum models toward anisotropic
67 emerging infilled-pattern generation, and describe its efficient im-
68 plementation. Second, we provide a comprehensive study on the
69 effect of the parameters in such an anisotropic context with a spe-
70 cific focus on providing explicit control over the averaged size and
71 elongation of microstructure cells. We demonstrate the applicabil-
72 ity of our approach to various shape-design applications such as
73 mechanical design and biology. Overall, we hope that such an ap-
74 proach simulating the emergence of natural forms will help and
75 inspire designers from various domains in their process of creating
76 more complex and organic-looking shapes.

77 The rest of the article is organized as follows. We start with a re-
78 view of the related work (Sect. 2) and background on the particle-
79 based model of the *Physarum* (Sect. 3). Section 4 presents an
80 overview of our generative method, followed by our technical con-
81 tributions for 3D oriented emerging patterns (Sect. 5) and param-
82 eter analysis (Sect. 6). We then present our results (Sect. 7) before
83 concluding.

84 2. Related Work

85 In Section 2.1, we delve into the topic of microstructure infill for
86 material design, as our method is closely tied to this field, particu-
87 larly in terms of efficient fabrication using Additive Manufacturing.
88 Furthermore, in Section 2.2, we address Bio-inspired Modeling and
89 specifically focus on the *Physarum polycephalum* as a compelling
90 model for our intended purpose.

91 2.1. Microstructures and shape infill for AM

92 The importance of internal fill patterns in additive manufacturing
93 has a long research history in mechanical engineering [AAD98].
94 By avoiding dense interior fills, both printing time and material us-
95 age can be significantly reduced. As a result, the initial infill pat-
96 terns were developed with the primary goal of reducing material
97 density while also being quick to generate and effective in produc-
98 tion.

99 Topology optimization, allowing the optimization of the distri-
100 bution of material within a given domain subject to a set of con-
101 straints, has been successfully used in a large range of applica-
102 tions as described in these reviews [BS03, WSG21]. Porous mate-
103 rial generation [WAWS18, SPG19] can, in particular, benefit from
104 high resolution topology optimization [AALS17], but remain com-
105 putationally prohibitive. Additional flexibility in the generated pat-
106 tern has been proposed by the use of post-process applied on top of
107 topology optimization result, such as the use of procedural func-
108 tions [PT08, AGDP19], or reaction-diffusion [GSR22].

109 Periodic structures, originally proposed by Sigmund [Sig95],
110 have also been widely explored to generate complex structures
111 featuring, for instance, targeted rigidity [ZSCM17], deformation
112 [TTZ*20], or balance [WWZW16]. Gradation of microstruc-
113 ture design can be achieved via the use of different tiles [PZM*15,
114 GWK*19], or regularized deformation [GDAP20]. Although peri-
115 odic microstructures are highly efficient, they depend on underly-
116 ing regular grids, which make them challenging to apply to mi-
117 crostructure with spatially varying orientation and curved bound-
118 aries. Moreover, graded or oriented periodic microstructures sel-
119 dom produce patterns with smooth connectivity at the interface be-
120 tween neighboring cells. This connectivity must thus be enforced
121 by introducing additional geometrical constraints onto the gener-
122 ated patterns.

123 Close to our approach, stochastic processes provide design
124 flexibility and progressive gradation since they are not restricted
125 by a grid or subdivision rule. They have been recently used
126 for foam-like microstructures [MDL16], and extended toward
127 anisotropic [MSDL17] shapes, polyhedral cells [MHSL18], or
128 lamellar structures [KTZK20]. Compared to fully periodic mi-
129 crostructures, the lack of a perfectly symmetric structure of
130 stochastic process has been reported to exhibit greater resistance to
131 fabrication imperfections [PVK*20, vEYC*21]. While 2D Voronoi
132 cells [LS03, LCL*21] can relate to physarum cell look, the direct
133 use of 3D Voronoi cells results in surfaces, generating membranes
134 instead of filaments as observed in our case. Voronoi cell edges
135 have been employed for foam modeling in previous works by Mar-
136 tinez et al. [MDL16, MSDL17], but we emphasize that these ap-

137 proaches exhibit polygonal structures with straight edges, lacking
138 the organic, curved shapes that our method generates natively.

139 Our approach can be described as a stochastic morphogenetic
140 process and relies on the local emergence of non-periodic mi-
141 crostructures spatially graded by orientation and density fields.
142 Compared to other stochastic approaches, it has the advantage of
143 relying only on local computation, thus avoiding computationally
144 expensive global optimization steps. In addition, the underlying
145 emerging process allows for generating flexible patterns that align
146 well with curved boundaries and can dynamically adapt to local
147 user modifications.

148 2.2. Bio-Inspired Modeling and Physarum polycephalum

149 Multi-scale structures are abundant in nature and can be observed
150 in various plant and animal organisms [Lak93, FW07]. Despite the
151 fact that their underlying conception processes are not always com-
152 pletely understood, they typically possess remarkable mechanical
153 properties. This has recently given rise to a new field known as
154 "Bio-Inspired Modeling" or "Bio-Inspired Design," which is com-
155 monly employed in the context of structural design for Additive
156 Manufacturing [DPBY*19, PMNWW19, ZWZ*20]. In contrast to
157 mathematical optimization, *Bio-Inspired Modeling* has its origins
158 in the field of morphogenesis and seeks to employ natural processes
159 to create optimized designs. Due to its interdisciplinary nature, it
160 is challenging to consider it as a singular design process. Rather,
161 it comprises various approaches that use different representations
162 and operate at different scales [CHK*05].

163 The "many-headed" slime mold, known as *Physarum poly-*
164 *cephalum* or "blob", was initially misclassified as a fungus, but
165 is actually a giant unicellular protist with multiple nuclei. First
166 described by [How31], this organism has been extensively stud-
167 ied in various fields including cell biology, biochemistry, genet-
168 ics, and more recently, physics. In recent years, it has gained in-
169 terest due to its remarkable properties. Hence, despite lacking a
170 brain, the unicellular organism is capable of decision-making and
171 spatial memory of its environment [RLDB12, BL15]. Furthermore,
172 akin to other self-organizing systems, the slime mold exhibits self-
173 repairing abilities [Ada13]. A seminal experiment conducted by
174 Japanese researcher Toshiyuki Nakagaki [NYT00] demonstrated
175 that the slime mold can find the shortest route through a maze.
176 Since then, many studies have investigated its maze-solving capa-
177 bility [NYT01, Nak01, ZZD11, NVSA17], and it has even been
178 shown to solve the Towers of Hanoi problem [RB13]. Its ability
179 to solve the Steiner tree problem [TNT*10] and thus to repro-
180 duce real-world infrastructure networks [TTS*10] has also been
181 explored.

182 While several models have been proposed to explain the
183 Physarum behavior such as mathematical equations on flux
184 [TKN07] or Cellular Automaton [TS12], we direct our attention
185 to a particle-based model introduced by Jeff Jones [Jon09, Jon10],
186 described more precisely in Section 3, due to its ability to gener-
187 ate intricate organic-looking structures. To the best of our knowl-
188 edge, only a few works extended this concept to three dimen-
189 sions. Jones [Jon15] himself described a brief exploration of three-
190 dimensional environments, followed by applications toward design

191 and architectures [MX17, DMM18], as well as for artistic appli-
192 cation in the *BioArt* concepts [Sch13, Que20, Bar09, Seb23]. These
193 approaches, however, provide only limited analysis of their model's
194 parameters. Additionally, this early 3D variant [Jon15] relies on
195 five samples for directional sensing (1 central, and 4 peripherals)
196 which leads to artifacts when applied to the anisotropic case, as
197 explained in Sect. 5.1.

198 The most recent extension of Jones' model in 3D, the so-called
199 *Monte Carlo Physarum Machine (MCPM)*, tailored for reconstruct-
200 ing and visualizing the cosmic web [BET*20, EBPF20a, EBPF20b,
201 EBPF22], introduces stochastic updates helping to produce highly
202 connected networks that align with cosmological data. This proba-
203 bilistic model offers an elegant and robust formalization, and con-
204 tains the deterministic Jones' model (called Max-PM by the au-
205 thors, and relying on 1 central and 8 peripheral sensing directions)
206 as its limit case. As stated in [EBPF22], Max-PM yields a clean,
207 well-defined structure, which however does not consistently cover
208 all the input cosmological data compared to the MCPM variant. Yet
209 in our case, the property of providing clean and well-defined struc-
210 ture is very well suited for shape modeling, in contrast with the pa-
211 rameterized fuzziness introduced by the MCPM variant. Nonethe-
212 less, we note that Ehrlich et al. [Ehr21, EHE22] have proposed
213 an application to additive fabrication based on the MCPM model.
214 If [Ehr21] limits the emergence of the pattern to a guiding mesh's
215 surface, [EHE22] demonstrates the infilling of a 3D helmet, close
216 to our volume-based pattern generation, but without the possibility
217 to control the local orientation. We propose to build on the simple
218 Max-PM model, with the addition of (i) rotation-invariant particles'
219 sensor sampling for a fully 3D consistent model; (ii) a more com-
220 prehensive control over the local infill structure using anisotropic
221 diffusion weights for precise oriented propagation behavior; (iii)
222 associated to a pattern cells size analysis, suitable for both aesthetic
223 application and additive manufacturing.

224 3. Background on Physarum Agent Based Model

225 Our methodology relies on an agent-based model of *Physarum*
226 *polycephalum*, originally proposed by [Jon10] for 2D simulation.
227 For the sake of clarity, we describe this existing model in this sec-
228 tion.

229 As illustrated in Figure 2, the model represents the *Physarum* as
230 a collection of agents $\mathcal{A} = \{a_k\}_{k \in \llbracket 1, N \rrbracket}$ that interact with a density
231 grid \mathcal{T} through a deposit/sensory behavior. Each agent a_k possesses
232 a location p_k , a heading direction u_k , and three front sensors, each
233 positioned at a distance r (Sensor Offset, denoted SO in the original
234 paper) from the particle. The front sensor is oriented in the heading
235 direction, and the positions of the left and right sensors are ob-
236 tained through a rotation of $\pm\varphi$ (Sensor Angle or SA) around p_k . \mathcal{T}
237 is stored as a 2D array of scalar values representing the marker (in
238 biological contexts usually referred to as chemoattractant) emitted
239 by the agents and is called the *trail map* as the density will evolve
240 toward showing the trajectory trails of the agents through the sim-
241 ulation. By using its sensors, each agent can read the trail map \mathcal{T}
242 and adjust its movement accordingly. The simulated evolution of
243 the model is obtained via discrete-time iterations, where both \mathcal{A}
244 and \mathcal{T} are updated according to a six-step rule (see Fig. 2):

1. **Sense.** Each agent starts by reading the density in the cells of

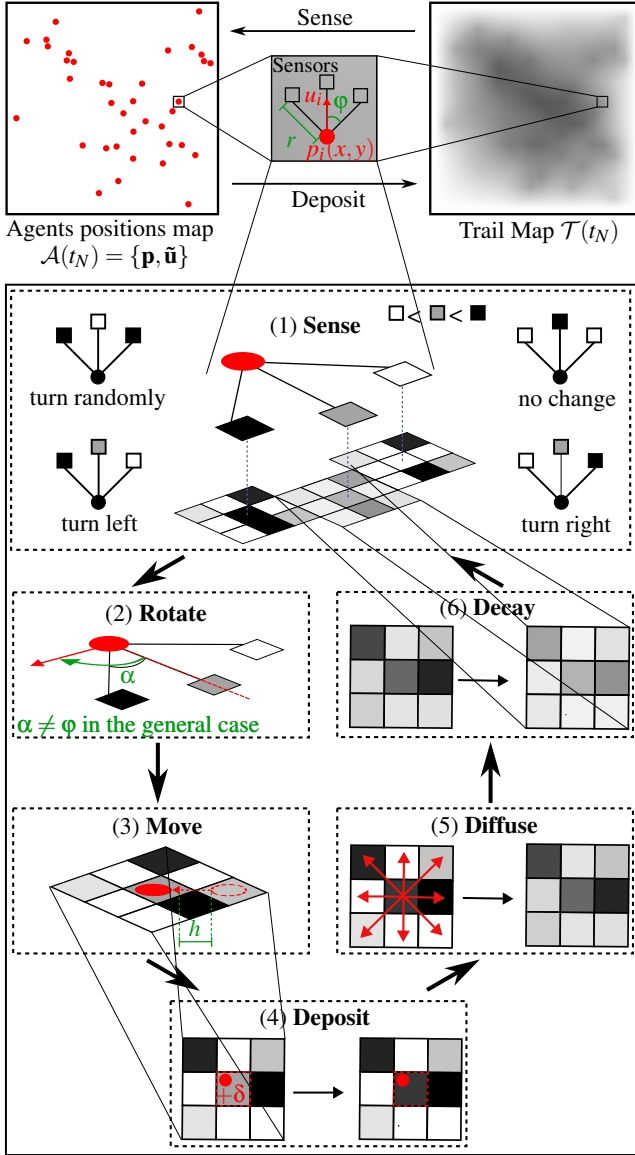


Figure 2: Jones' Physarum model.

- 260 5. **Diffuse.** The trail diffuses according to the diffusion equation
 261 $\frac{\partial \mathcal{T}}{\partial t} = d \Delta \mathcal{T}$ during a short time frame.
 262 6. **Decay.** A temporal decay is modeled by damping the diffusing
 263 values of \mathcal{T} by μ (typically 0.1) : $\mathcal{T} \rightarrow (1 - \mu)\mathcal{T}$.

264 Jones's original paper includes a collision detection step that guar-
 265 antees the presence of at most one particle within each grid square.
 266 Measures of space availability (growth of the population of agents)
 267 and overcrowding (adaptation by population reduction) are also in-
 268 troduced later [Jon15]. These steps are essential for faithfully emu-
 269 lating the behavior of *Physarum polycephalum*, yet they do not cru-
 270 cially affect the patterns produced and we don't implement them in
 271 our approach. Additionally, avoiding this collision detection conveni-
 272 ently eliminates any sequential dependence, enabling enhanced
 273 computational parallelism. In practice, starting from a random dis-
 274 tribution of agents, the emergence of patterns is observed after
 275 about a few hundred steps and leads to a relatively stable configura-
 276 tion around a few hundred steps. An exhaustive study of the effect
 277 of the different parameters (r , h , α , ϕ , agents population size s ,
 278 decay value μ ,...) on the pattern formation can be found in the found-
 279 ing paper [Jon10]. According to Jones, the transition from 2D to 3D
 280 sensors can be conceptualized as a shift from a flat anchor shape to
 281 a three-dimensional "grappling hook" shapes with four hooks. In
 282 our work, we expand upon this concept by adopting a 3D grappling
 283 hook shape with more hooks. Furthermore, we introduce the capa-
 284 bility to confine pattern formation within a specific area and modify
 285 the diffusion equation to account for anisotropy. This modification
 286 enables the generation of oriented microstructures.

287 4. Method Overview

288 Given a set of initial parameters (Fig. 3-left), the agent-based simu-
 289 lation updates the set of particles $\mathcal{A} = \{a_k\} = \{p_k, u_k\}$, where p_k
 290 represents their positions and u_k denotes their heading directions.
 291 Each particle can move and deposit a small amount of material den-
 292 sity on the trail map \mathcal{T} , creating a network of patterns over time
 293 (Fig. 3-middle). The final shape surface is obtained by computing
 294 an isovalue of the trail \mathcal{T} (Fig. 3-right), typically using techniques
 295 such as marching cubes or dual contouring when a triangular mesh
 296 is required for visualization and manufacturing purposes.

297 In order to generate oriented microstructures that infill a guiding
 298 shape defined as a boundary surface \mathcal{B} , we introduce three specific
 299 input fields defined on a rectangular domain $\Omega \subset \mathbb{R}^3$, namely, an
 300 infill space field \mathcal{I} , a tensor field \mathbf{D} , and a guiding trail \mathcal{T}^* .

301 **Infill Space Field \mathcal{I} .** The scalar field $\mathcal{I}(\mathbf{x} \in \Omega)$ is used to im-
 302 plicitly define the space where the microstructures grow as $\mathcal{D}_{\mathcal{I}} =$
 303 $\{\mathbf{x} \in \Omega \mid \mathcal{I}(\mathbf{x}) > 0\}$. In practice, we consider \mathcal{I} to be a simple bi-
 304 nary field (1 inside and 0 outside) or a signed distance function to
 305 the boundary surface.

306 **Tensor field \mathbf{D} .** The tensor field $\mathbf{D}(\mathbf{x} \in \Omega)$ indicates the desired
 307 local orientation and local anisotropy of the microstructures. It can
 308 be derived from specific data available to mechanical engineering
 309 such as desired stress, or from a direct user's defined orientation
 310 field. \mathbf{D} is used as a diffusion tensor in the **Diffuse** step and tends
 311 to align the cell-like and filament-like patterns with its principal
 312 direction, and its parameterization will be described in Sect. 6.1.

246 \mathcal{T} corresponding to the positions of its three sensors. The agent
 247 turns toward the direction of the sensor with the highest density
 248 and takes a random one in case of equality. As a consequence,
 249 the agents are sensible to the gradients of trail. During this sensor
 250 reading step only, \mathcal{T} can be weighted with another density
 251 array, allowing to incorporate input data such as fixed attractive
 252 areas.

- 253 2. **Rotate.** In case of change of direction, the heading vector of the
 254 agent is then rotated from an angle α (Rotation Angle or RA).
 255 Note that in general $\alpha \neq \phi$.
 256 3. **Move.** The agent moves along its updated heading direction of
 257 a distance h (Step Size or SS).
 258 4. **Deposit.** The agent located in p_k adds a small amount of density
 259 δ in the corresponding grid square of \mathcal{T} .

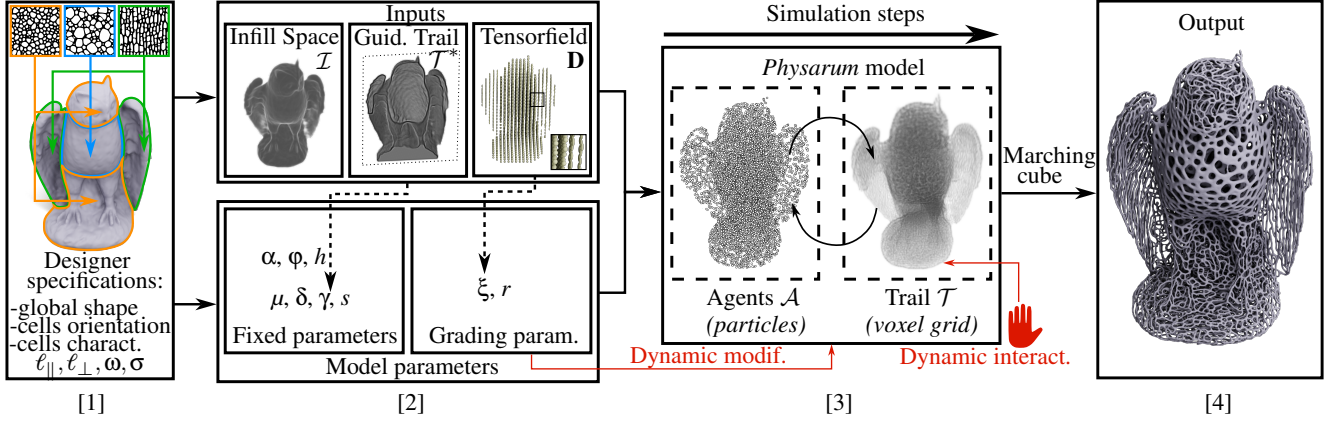


Figure 3: Overview of our approach. [1] User defined constraints: Global shape domain with cell’s local orientation and characteristics. [2] Expression of the constraints as models parameters: Infill domain (\mathcal{I}), anisotropic behavior (\mathbf{D}), and boundary conditions (\mathcal{T}^*), that can be associated to spatially varying parameters to generate different local pattern aspects. Other simulation parameters are fixed. [3] The Physarum simulation evolves through iterations leading to the emergence of microstructure patterns on the output Trail map \mathcal{T} stored in a grid structure. Interactive modifications from the user can be applied at any time, either via the change of the model parameters, or on the evolving Trail map. [4] A final mesh surface representing a porous structure can be extracted from the trail map using marching cube. Grid size for the Trail map \mathcal{T} : $370 \times 306 \times 534$.

313 **Guiding Trail \mathcal{T}^* .** The scalar field $\mathcal{T}^*(\mathbf{x}) \in [0, 1]$ is used to enforce the pattern formation in specific areas. The *guiding trail* operates during the **Sense** step, we set the sensors to read an *effective density field*

$$\mathcal{T}^\gamma = (1 - \gamma)\mathcal{T}^0 + \gamma\mathcal{T}^*, \quad (1)$$

317 given as a linear interpolation between the normalized trail $\mathcal{T}^0 = \frac{\mathcal{T} - \min \mathcal{T}}{\max \mathcal{T} - \min \mathcal{T}}$ in $[0, 1]$, and \mathcal{T}^* . The weight γ is a fixed value chosen in $[0, 1]$ which controls the influence of \mathcal{T}^* . Because of their sensing behaviour, the agents are sensible to the local variations of the *trail*, which means that attractive areas of \mathcal{T}^* are indicated by its gradient toward its high value. Note that unlike \mathcal{T} , the *guiding trail* \mathcal{T}^* does not evolve during the simulation, therefore facilitating consistent pattern formation in specific areas. While we can not give a general formulation for \mathcal{T}^* since it is provided by the user as input, we can define it within a specific use case. A common use of \mathcal{T}^* is the creation of an outer shell of thickness ϵ encouraging pattern formation along the curved boundary. Let us call $d(\mathbf{x}, \mathcal{B})$ the closest Euclidian distance between \mathbf{x} to the boundary \mathcal{B} , in that case \mathcal{T}^* can typically be defined as a characteristic function

$$\mathcal{T}^*(\mathbf{x}) = \mathbb{1}_{\{x, d(x, \mathcal{B}) < \epsilon\}} \quad (2)$$

337 which creates a gradient of trail toward this area, illustrated Fig. 4.

338 While we call these three fields inputs, other parameters involved in the model (sensor values, guiding influence, decay factor, etc) can also vary spatially. We will call them *grading parameters* and

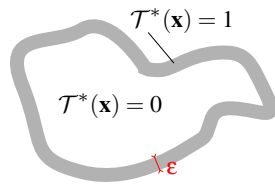


Figure 4: Typical \mathcal{T}^* .

341 provide a guideline in Sect. 6 to set their values depending on the expected pattern appearance.

343 5. Efficient 3D oriented Physarum Model

344 We describe in the following the specific modification we apply in the Physarum model in order to efficiently simulate its emergence in a 3D spatial environment in the anisotropic case.

347 5.1. Spatial sensing

348 The first essential element for 3D Physarum growth is to extend the agents’ sensors into a 3D structure. Figure 5 showcases different possible layout for this. A natural extension consists in adding sensors associated with the rotation of the 2D basic layout around its heading direction. This leads to these n -legs grappling hook-looking shapes with 1 central sensor and n peripheral, that we call $\{1 + n\}$ layout. Fig. 5 shows that n has to be sufficiently high (typically ≥ 8) to consistently sample the circle produced with the sensors and avoid any artifacts in the anisotropic case. Increasing n beyond 10 has no real impact on the generated structures. Previous early attempts on 3D Physarum models [Jon15, MX17] (respectively $\{1 + 4\}$, $\{1 + 4 \times 2\}$ layouts Fig. 5) used only four sampling directions which leads to directional artifacts in anisotropic representations due to the lack of angular sampling. Uniform sampling on a hemisphere could also be considered, but comparing the results given by the $\{1 + 8\}$ and the Unif. $\{9\}$ layouts shows that uniform distribution does not generate better aligned and clean cells. Moreover when the number of uniformly distributed sensors increases (Unif. $\{40\}$ Fig. 5), the model changes of behavior and tend to always keep their heading direction aligned with the anisotropy direction leading to filament structures. As a result, the non-continuous sampling offset allows to form stable oriented

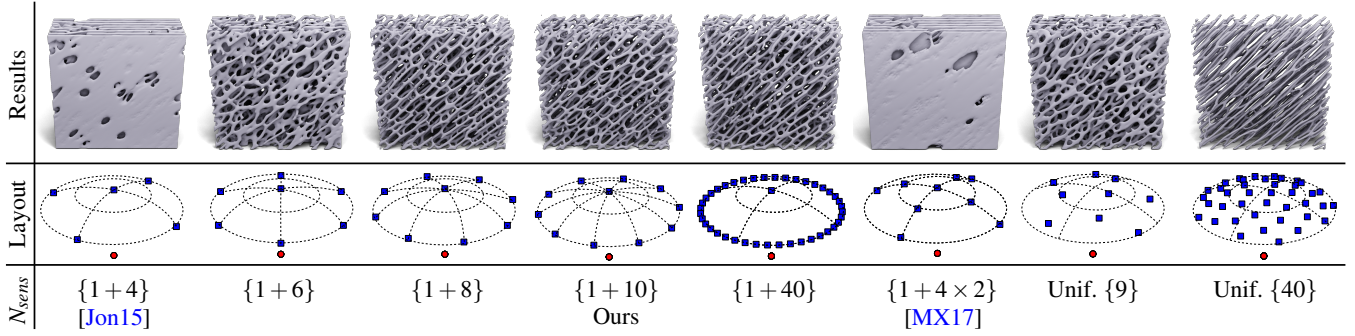


Figure 5: Resulting anisotropic structures for different 3D sensors layout, with parameters $r = 3$ and $\xi = 4$ (parameter introduced Section 6.1) generated on a $200 \times 200 \times 70$ grid. From left to right, the five first layouts $\{1+n\}$ are n -legs grappling hook-looking shape with increasing n , $n = 4$ being the layout proposed by [Jon15]. $\{1+4 \times 2\}$ layout comes from [MX17]. In the last two layouts Unif. $\{n\}$, n sensors are uniformly distributed on the hemisphere using the Fibonacci Sphere.

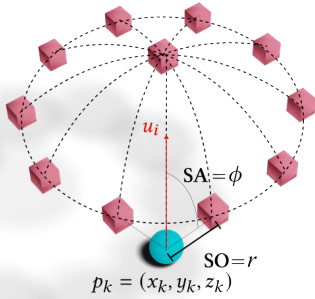


Figure 6: Agent and its sensors in 3D.

370 foam-cell structures, which is also why we do not rely on continuous probabilistic distribution sampling such as in [EBPF20a]. In all
371 our examples we used the $\{1+10\}$ layout showed Figure 6.
372

373 5.2. Infill Space Restriction

374 To confine the pattern generation within a 3D shape described by
375 the infill space $\mathcal{D}_{\mathcal{I}}$, we add a positional constraint after the step
376 **Move**. In practice, we check at each frame the value of $\mathcal{I}(p_k)$
377 for each agent's position p_k . If $\mathcal{I}(p_k) \leq 0$, the position is outside of the
378 shape, then we project it back along its backward heading direction
379 $p_k - u_k \Delta t$, where Δt is the simulation time step. This yet simple
380 approach proved to be sufficient to deal with boundaries without
381 accumulation as the trail is diffused and is mixed with the guide
382 \mathcal{T}^* near the border \mathcal{B} .

383 5.3. Anisotropic patterns

384 The local pattern orientation can be controlled by the anisotropic
385 tensor \mathbf{D} given as input. In the **Diffuse** step, the trail is diffused
386 according to the anisotropic diffusion equation

$$\frac{\partial \mathcal{T}}{\partial t} = \nabla \cdot (\mathbf{D} \nabla \mathcal{T}). \quad (3)$$

387 This modified equation results in patterns that align with the input
388 tensor field. Specifically, the cells/filaments tend to follow the
389 direction indicated by the eigenvector of \mathbf{D} corresponding to the
390 highest eigenvalue.

391 Care has to be taken when integrating anisotropic diffusion using
392 discrete finite differences. Indeed, the use of the classical centered
393 differences on a regular grid has greater accuracy along the main
394 directions. While hardly visible for isotropic diffusion, this leads to
395 strong artifacts when oriented patterns need to be generated in non-
396 axis-aligned directions. To address this issue, we propose a solution
397 by generating at each frame a 3D rotation R randomly oriented on
398 the unit sphere, and applied to both the trail map and the tensor
399 field \mathbf{D} before computing the **Diffuse** step. Once computed, the up-
400 dated trail map is transformed back in applying the inverse rotation
401 R^{-1} . By doing so, we can effectively handle any direction in a con-
402 sistent manner while still utilizing the simplicity of a regular grid.
403 It is important to note that this approach does not aim at improv-
404 ing numerical accuracy for the diffusion process but provides an
405 orientation-invariant one, which is sufficient for our purpose.

406 5.4. Local block-based synthesis

407 Generating microstructures on a large-scale domain at once can be
408 memory intensive. To avoid memory shortage in such case, we pro-
409 pose a per-block synthesis approach leveraging the local behavior
410 of the physarum coupled with the guiding-trail input \mathcal{T}^* . As illus-
411 trated in Fig. 7, the global domain Ω can be split into blocks Ω_i
412 with small overlapping areas on their boundary. The interior of the
413 blocks is filled independently, one after the other, while ensuring a
414 coherent boundary condition. This condition is ensured by copying
415 the value of the trail of the filled neighbors block (Ω_1 in Fig. 7)
416 on the overlapping domain into the guiding trail map \mathcal{T}^* of the
417 block to be filled (Ω_2 in Fig. 7). This technique can scale to an
418 arbitrary range and level of subdivision as long as the block size
419 is sufficiently large compared to the typical length of a cell pat-
420 tern. Therefore physarum structures can be generated on grids of
421 any size using this approach. As shown Fig. 8, visual artifacts in-
422 troduced by this process are minor if non-existent, as long as the

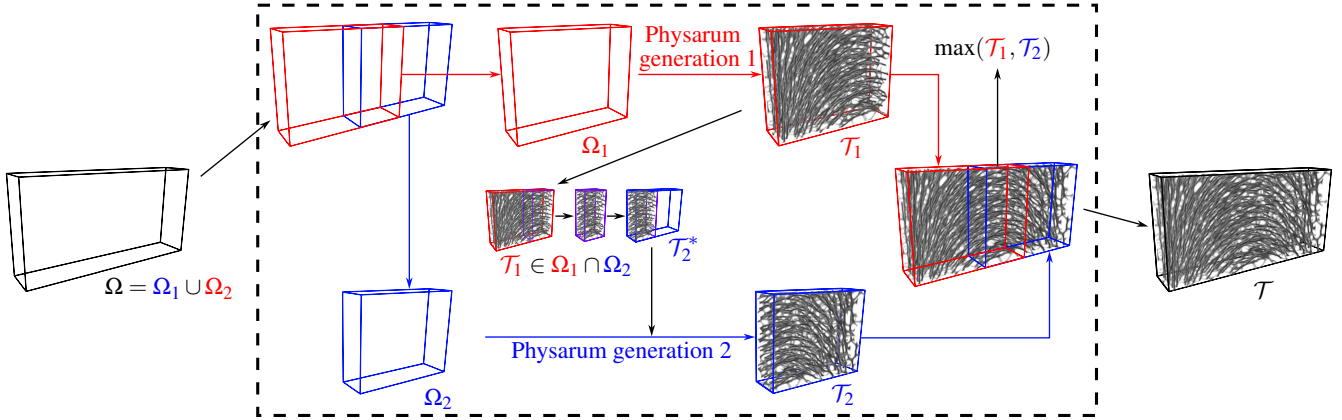


Figure 7: Per-block synthesis allows locally synthesizing a physarum structure and coupling it to nearby blocks via their common boundary.

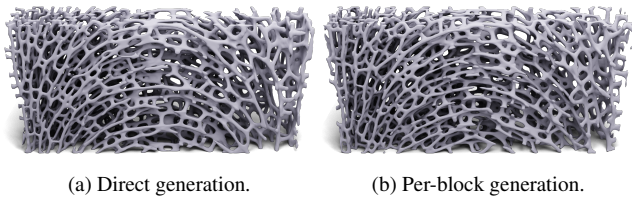


Figure 8: Physarum structure generated directly on the whole grid (a) and using the local block approach shown Fig. 7 (b). Grid size : $400 \times 200 \times 70$.

447

$$\omega = \frac{\ell_{\parallel}}{\ell_{\perp}}, \quad \sigma = \ell_{\parallel} \ell_{\perp}^{d-1}, \quad (4)$$

448

449

450

451

with $d = 2$ or 3 according to the dimension, and where ℓ_{\parallel} and ℓ_{\perp} are the averaged cell lengths in the most elongated, and least elongated directions.

452

453

454

455

456

457

458

459

While ℓ_{\parallel} and ℓ_{\perp} , and thus of ω and σ , can be directly computed by direct minimal and maximal length measurement over closed cells in 2D, their computation is not straightforward in 3D as the cells are not associated to bounded sub-domains. We propose a common computation methodology that can be applied to both two-dimensional and three-dimensional structures in relying on the apparent frequencies of the trail map.

Let us call

$$f_{\parallel} = \frac{L}{\ell_{\parallel}}, \quad \text{and} \quad f_{\perp} = \frac{L}{\ell_{\perp}}, \quad (5)$$

460

461

462

463

464

465

466

467

468

469

470

471

472

473

474

the frequencies corresponding to the averaged cell length in the respective most and least elongated directions. Here, L designates the total length of the square/cubic domain. These two frequencies are the most apparent and, therefore, correspond to local peaks of magnitude in the spectrum of the trail map. To compute f_{\parallel} and f_{\perp} , we perform a Fast Fourier Transform on the output trail and consider a frequency as being locally dominant if its magnitude in the Fourier spectrum is higher than a certain percentage p of the local maximum magnitude. For values of p chosen between 25% and 75%, values of f_{\parallel} and f_{\perp} are translated by a similar offset, but their behavior remains the same. In all of our experiments, we chose $p = 37\%$ as this value gives elongation values that match a direct elongation computation in the 2D case for closed cells.

In the following, all numerical values are obtained using the parameters provided in the summary Table 1.

6.1. Diffusion ratio ξ and tensor parameterization

The diffusion tensor field \mathbf{D} can be defined from specific data provided by the designer, such as desired mechanical properties, ori-

423

424

425

426

427

428

429

430

431

432

433

434

435

436

437

438

439

440

441

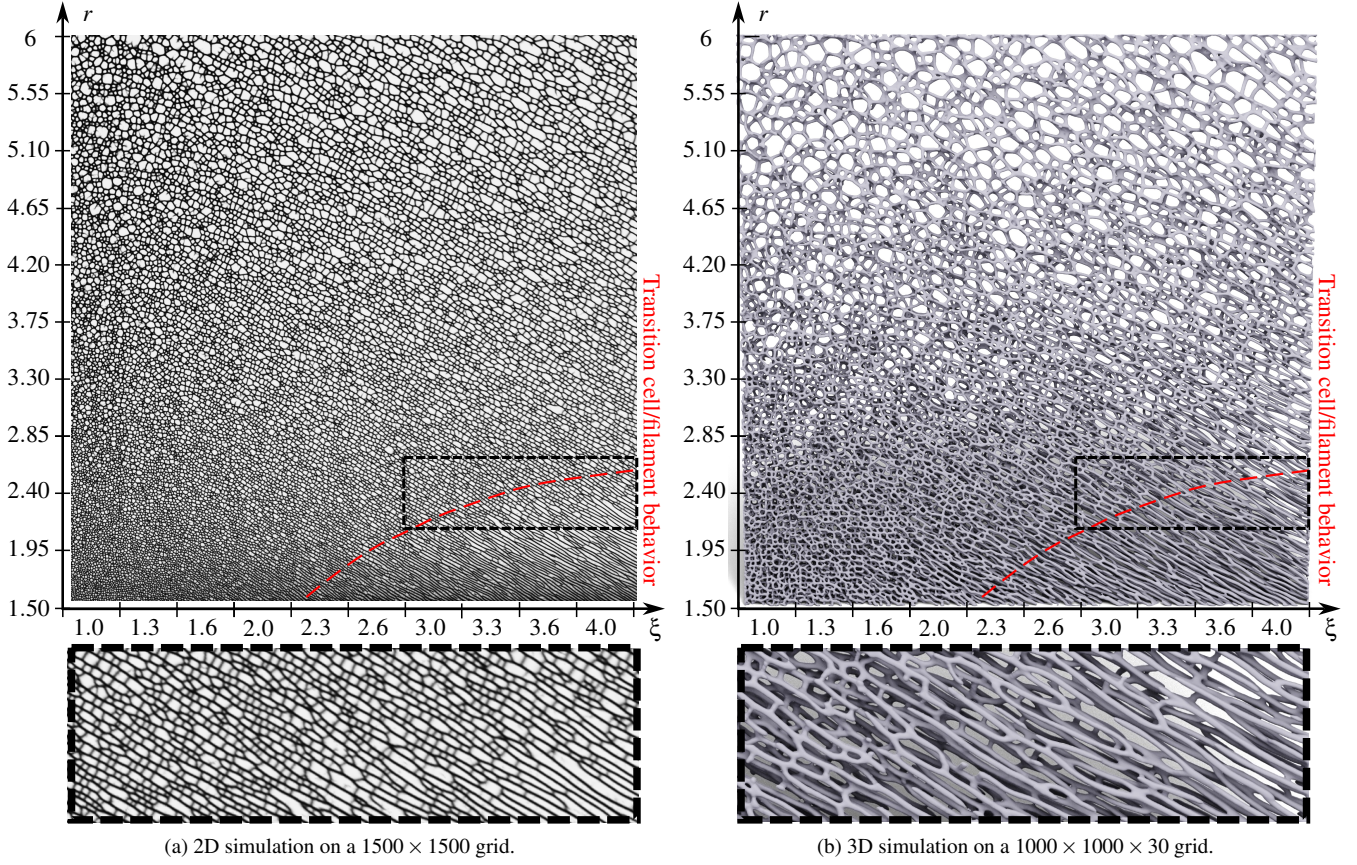
442

443

444

445

446

Figure 9: Patterns obtained for varying values of ξ and r .

Param.	Designation	Pattern affect	Values
ξ	Diffusion ratio	Elongation ω Fil. behavior ($r \leq 2.5$)	$[1, 2.5]$ $[2.5, 4]$
r	Sensor Offset	(ω, σ) Fil. behavior ($\xi \geq 2.5$)	$[2.5, 6]$ $[1.5, 2.5]$
φ	Sensor Angle	Pattern aspect	27°
α	Rotation Angle	Pattern aspect	70°
h	Step Size	Pattern formation	1
μ	Decay	Scaling, edge thickn.	0.1
δ	Deposit	Trail scaling	0.01
γ	Guid. influence	Influence of \mathcal{T}^*	$[0, 1]$
s	Pop. size	Pattern formation	$[2, 4]$

Table 1: Summary of the Physarum parameters, respective influence, and typical values. The values of r and h are given in pixel/voxel.

483 a diffusion ratio $\xi(\mathbf{x})$, $\mathbf{x} \in \Omega$, guiding how much the cells should be
 484 elongated along this principle direction. In the following, we will
 485 assume that we restrict our model to elongated cells in a single di-
 486 rection in space, while assuming a transversal isotropy in the two
 487 remaining orthogonal directions

488 The 3×3 diffusion tensor matrix \mathbf{D} can be decomposed at any
 489 position $\mathbf{x} \in \Omega$ as

$$\mathbf{D}(\mathbf{x}) = \mathbf{R}_o^T(\mathbf{x}) \mathbf{\Lambda}_\xi^T(\mathbf{x}) \mathbf{\Lambda}_\xi(\mathbf{x}) \mathbf{R}_o(\mathbf{x}), \quad (6)$$

490 where $\mathbf{R}_o(\mathbf{x})$ is a rotation matrix defining a local orientation frame
 491 for the diffusion, and $\mathbf{\Lambda}_\xi(\mathbf{x})$ is a diagonal matrix whose entries are
 492 the eigenvalues of $\mathbf{D}(\mathbf{x})$. The matrix $\mathbf{R}_o(\mathbf{x})$ can be defined from
 493 the directional vector $o(\mathbf{x})$ as $\mathbf{R}_o(\mathbf{x}) = (o(\mathbf{x}), o_1^\perp(\mathbf{x}), o_2^\perp(\mathbf{x}))$, where
 494 (o_1^\perp, o_2^\perp) can be arbitrarily oriented as long as they form an or-
 495 thonormal frame. The matrix $\mathbf{\Lambda}_\xi(\mathbf{x})$ can be defined as

$$\mathbf{\Lambda}_\xi(\mathbf{x}) = d_0 \text{diag}(\xi(\mathbf{x}), 1, 1), \quad (7)$$

496 where $d_0 \in \mathbb{R}$ is a diffusion magnitude, and $\xi(\mathbf{x}) \geq 1$ is the diffusion
 497 ratio.

498 ξ has a direct influence on ω as increasing the diffusion ratio
 499 leads to longer cells in the principal direction provided by o . Both ξ
 500 and o are then considered as input parameters to control the result of
 501 the simulation. The value d_0 has a direct influence over the cell size

478 entation, stress, and so on, resulting in a generated structure in ac-
 479 cordance with these properties. We propose to parameterize this
 480 diffusion tensor using, first, a normalized vector field $o(\mathbf{x})$, $\mathbf{x} \in \Omega$,
 481 with $\|o(\mathbf{x})\| = 1$ describing this main direction of diffusivity, and
 482 thus the principal direction of the elongation of cells; and second,

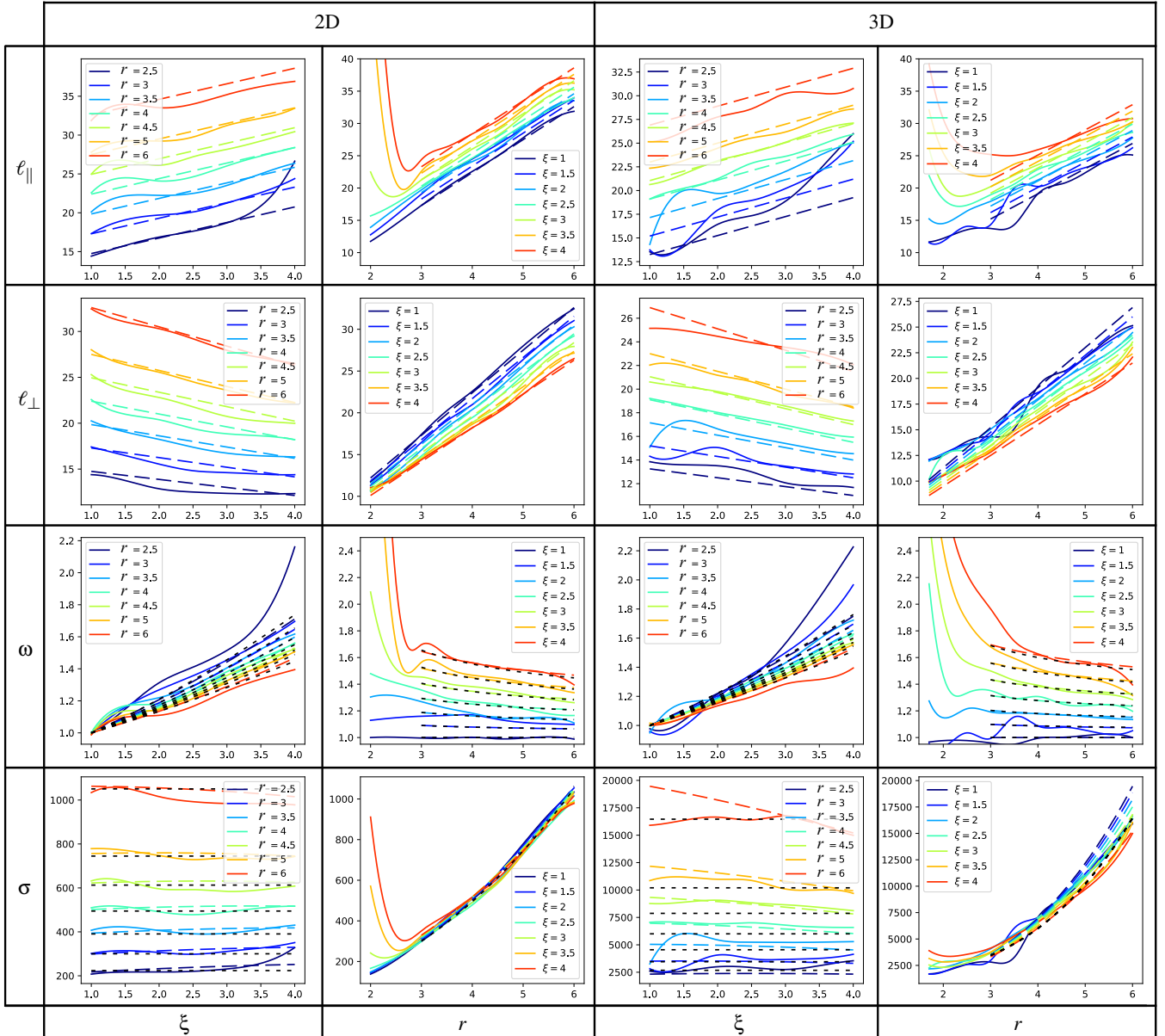


Figure 10: Plots of $(\ell_{\parallel}, \ell_{\perp}, \omega, \sigma)$ as a function of (ξ, r) , in 2D and in 3D. Dashed color curves are the fitting curves for ℓ_{\parallel} and ℓ_{\perp} , and the resulting ones for ω and σ , at the extreme values where our proposed numerical model is valid for cells patterns (i.e. where ℓ_{\parallel} is defined, for $\xi \in [1, 4]$, $r \in [3, 6]$). Values outside these intervals (darker blue curve of columns 1 and 3, leftmost part of columns 2 and 4) represent filament patterns. Black dotted curves for ω and σ are fitting curves with a more simple model provided equation 16.

502 since a large diffusivity leads to larger cells. However, the range
 503 of possible values of d_0 is limited by the stability of the numerical
 504 scheme to solve Eq. (3). Using an explicit scheme and a maximal
 505 diffusion ratio $\xi \simeq 4$ leads to a value d_0 that cannot exceed 0.2
 506 (assuming a discrete time step and spatial discretization set to 1).
 507 Based on this limitation, we consider d_0 to be a constant and set it
 508 to 0.1375.

509 6.2. Controlling cells characteristics

510 The second parameter to influence the cell size is the sensor offset
 511 r . At the opposite of d_0 , r is not restricted by numerical stability
 512 condition, and we therefore use it as a varying input variable. In the
 513 following, we analyze the influence of the two inputs (ξ, r) toward
 514 the cell characteristics $(\ell_{\parallel}, \ell_{\perp}, \omega, \sigma)$.

515 We first illustrate in Fig. 9 the typical patterns obtained for vary-
 516 ing values of ξ and r . While ξ acts primarily on the elongation of
 517 the patterns, r directly controls their global size. The dotted red line

delimits the two domains with different behaviors: the filament-like pattern in the bottom-right, and foam-like patterns. The foam-like patterns are obtained for moderate anisotropy relative to the cell size. In this configuration, the cells are characterized by long edges oriented along the main direction that increase with ξ , and a few orthogonal edges which lead to this typical foam-cell appearance. When the anisotropy becomes large ($\xi \geq 2.5$) while keeping a narrow cell ($r \leq 2.5$), the edges orthogonal to the main anisotropic direction are not able to emerge persistently anymore. As a result, the generated patterns are then dominated by long edges propagating along the principal direction that doesn't appear to be made of cells but look like long filaments instead.

In Fig. 10, we provide a finer analysis of the relation between $(\ell_{\parallel}, \ell_{\perp}, \omega, \sigma)$ plotted as functions of (r, ξ) . These curves can be used as an abacus to finely set a prescribed cell size and elongation. Let us first consider the parametric subdomain where $r \in [3, 6]$, $\xi \in [1, 4]$. This domain corresponds to foam-cell patterns where the characteristic cell lengths can be well predicted by our inputs using simple model. As we can see on the first line of the plots Fig. 10, at the first order, the elongation length ℓ_{\parallel} can be approximated by having a linear dependence to ξ and to r independently. The transverse length ℓ_{\perp} can be approximated by having a linear dependence to r , with a slope value that linearly decreases with ξ . We propose the following numerical model that approximate this behavior as

$$\begin{cases} \ell_{\parallel}(\xi, r) &= a_{\parallel} \xi + b_{\parallel} r + c_{\parallel} \\ \ell_{\perp}(\xi, r) &= a_{\perp} \xi r + b_{\perp} r + c_{\perp}, \end{cases} \quad (8)$$

with an additional condition on the elongation:

$$\forall r, \quad \omega(1, r) = \frac{\ell_{\parallel}(1, r)}{\ell_{\perp}(1, r)} = 1, \quad (9)$$

describing the fact that the cells are not elongated in the isotropic case. This gives a relation between the previous coefficients:

$$\begin{cases} a_{\parallel} + c_{\parallel} = c_{\perp} \\ b_{\parallel} = a_{\perp} + b_{\perp}, \end{cases} \quad (10)$$

which allows to eliminate two coefficients to re-write the expressions under the form:

$$\begin{cases} \ell_{\parallel}(\xi, r) &= a_0 \xi + (a_1 + a_2) r + a_3 \\ \ell_{\perp}(\xi, r) &= (a_1 \xi + a_2) r + (a_0 + a_3). \end{cases} \quad (11)$$

with values fitted using simple regression, for the 2D and the 3D cases,

$$\begin{cases} 2D : a_0 = 2.0, a_1 = -0.35, a_2 = 5.4, a_3 = 0 \\ 3D : a_0 = 2.0, a_1 = -0.30, a_2 = 4.2, a_3 = 1.5 \end{cases} \quad (12)$$

The behavior is similar in 2D and 3D but the fitting coefficients slightly differs between the dimension. Still, they remain close enough to assimilate these numerical differences to the fact that 2D cells and 3D cells are not completely comparable as they define slightly different structures and the 3D case exhibits wider degree of freedom to measure ℓ_{\parallel} and ℓ_{\perp} .

Overall, characteristic lengths of foam cells behave in the same way in 2D and 3D. ℓ_{\parallel} increases with ξ ($a_0 > 0$) and with r ($a_1 + a_2 > 0$) which is to be expected. ℓ_{\perp} also increases with r ($a_1 \xi + a_2 > 0$) but it decreases with ξ ($a_1 < 0$) meaning the anisotropy tends to bring the pattern closer in the transverse direction. For $r \leq$

3 and $\xi \geq 2.5$, the behavior changes to filament-like patterns. This change of behavior is also visualized on the plots, with a sudden increase of ℓ_{\parallel} values. Our model is still valid for ℓ_{\perp} because this length is still well defined in the filament behavior. These simple linear models are only first order approximation, and we may note for instance consistent local maxima for low ξ values (for ℓ_{\parallel}), that we neglect in such fitting.

ω and σ can also be well approximated using our proposed model for ℓ_{\parallel} and ℓ_{\perp} (dashed color curves Fig. 10). To really understand how ξ and r influence these characteristics, we re-write their expressions differently:

$$\omega(\xi, r) = 1 + \frac{\xi - 1}{r} f(\xi, r), \quad (13)$$

with

$$f(\xi, r) = \frac{a_0 - a_1 r}{a_1 \xi + a_2 + \frac{a_0 + a_3}{r}}, \quad (14)$$

and

$$\sigma(\xi, r) = (a_1 + a_2) a_2^{d-1} r^d + g(\xi, r), \quad (15)$$

with $g(\xi, r)$ a rational polynomial that we do not fully develop and $d \in \{2, 3\}$ corresponding to the dimension (2D or 3D).

In practice we observe that we can approximate $f(\xi, r)$ to be linearly varying with ξ and with r independently, and that $g(\xi, r)$ can be approximated by a constant σ_0 as its variation is negligible in front of $(a_1 + a_2) a_2^{d-1} r^d$. Finally the cell elongation and area/volume can be approximated by:

$$\begin{cases} \omega(\xi, r) &= 1 + \frac{\xi - 1}{r} (\alpha_0 \xi + \alpha_1 r + \alpha_2) \\ \sigma(\xi, r) &= (a_1 + a_2) a_2^{d-1} r^d + \sigma_0, \end{cases} \quad (16)$$

with values fitted using simple regression, for the 2D and the 3D cases,

$$\begin{cases} 2D : \alpha_0 = 0.045, \alpha_1 = 0.08, \alpha_2 = 0.24, \sigma_0 = 50 \\ 3D : \alpha_0 = 0.040, \alpha_1 = 0.11, \alpha_2 = 0.20, \sigma_0 = 1600 \end{cases} \quad (17)$$

This corresponds to the plots of the black dotted curves for ω and σ Fig. 10. Under this form, this shows clearly that the elongation can be approximated by having a quadratic relation to ξ , which can be linked to the square of ξ found in the expression of $\mathbf{D}(\mathbf{x})$. The influence of ξ tends to diminish while r increases, as the invert of r appears in the expression, with the other coefficients being positive. This is also to be expected because as r increases, the size of pattern increases, but not the radius of diffusion, therefore anisotropic diffusion is less likely to affect larger patterns. The cell area/volume is governed by the quadratic/cubic term r^d in σ , which is also coherent with the expected influence of r .

6.3. Fixed parameters for patterns formation

Beyond ξ and r used as *grading parameters*, other simulation parameters may influence how well patterns are defined. We briefly review in the following the influence of these additional parameters and propose the appropriate values we have been considering in addition to their summary in Table 1.

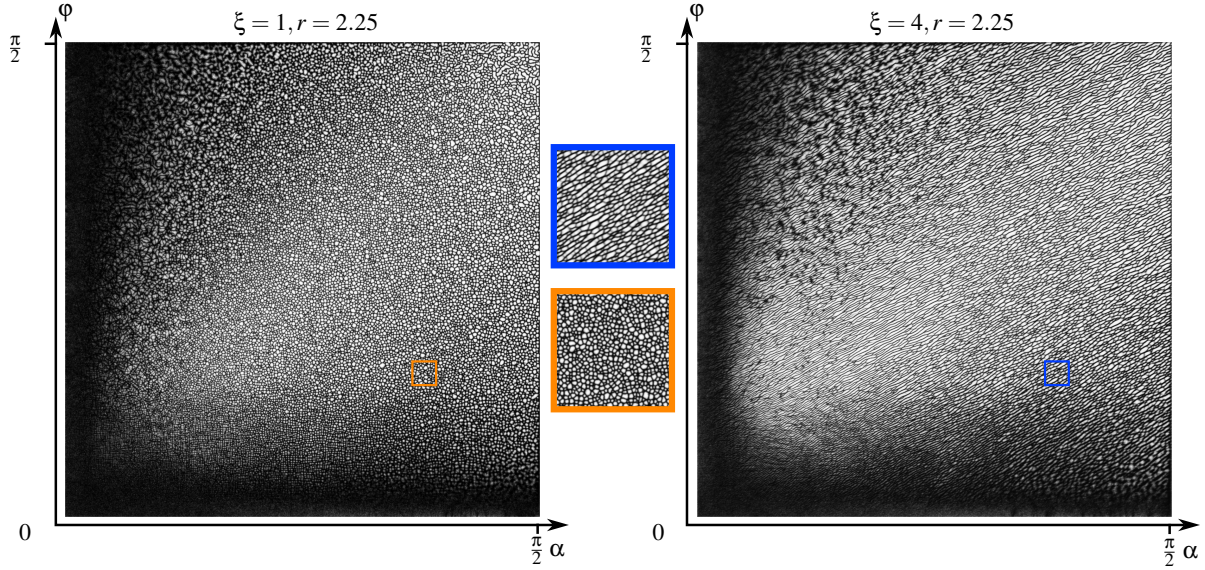


Figure 11: *Physarum* 2D pattern with α continuously varying along the x axis and ϕ continuously varying along the y axis, for isotropic (left) and anisotropic cases (right).

600 **Rotation angle α and Sensor Angle ϕ** have a significant influence on the appearance and formation of patterns. Jones [Jon10] proposed the general rule of $\alpha = 2\phi$, with typical value $\alpha = 45^\circ$, $\phi = 22.5^\circ$. We, however, note that the region where the foam-cell pattern appears consistently is narrower in the anisotropic case, and can lead to a mix of filament patterns when using $\alpha = 2\phi$. This behavior can be seen in Fig. 11 illustrating the patterns obtained along a continuous variation of ϕ and α between $[0, \pi/2]$ in both isotropic ($\xi = 1$, left), and anisotropic case ($\xi = 4$, right). The square illustrates the typical area providing foam-cells generation with consistent density in isotropic and anisotropic cases. This area corresponds to the ratio $\alpha = 2.6\phi$ and the typical considered values in our case are respectively $\alpha = 70^\circ$, $\phi = 27^\circ$.

613 **Pattern formation: Agent population, Step Size.** In all our simulation, the agents are initially uniformly distributed. The number of agents as well as the step size both impact the possibility of the microstructure being generated. Too low or high-value results in either non-connected structure or dense infill. We note that the sensibility of the simulation is higher when using large anisotropy, and normalized them as follows. First, the total agent population N is normalized by the ratio $s = N/V$, where V is the volume of the infill space. We found that values between $s = 2$ and $s = 4$ give satisfying results in all our cases. In fact, in 3D, satisfying results can be obtained with lower values i.e. for $s \geq 0.5$, which is very convenient from a computational cost. We assume that s does not need to be as high in 3D than in 2D because 3D shapes are much more porous than 2D shapes, while similarly connected. Second, the Step Size h is set to 1 pixel of the trail map image \mathcal{T} .

628 **Scaling factors: Decay μ , Deposit δ .** These two parameters do not change the type of pattern, but only act as scaling factors. While deposit δ simply scale the trail density value \mathcal{T} uniformly, the decay μ slightly change at the extreme values near 0 and 1 the thickness

632 of the edges on the trail map. We consider in all our experiment $\mu = 0.1$ and $\delta = 0.01$.

634 **Grid size.** As parameters such as r , h and the diffusion radius are defined in pixels or voxels, the resolution of the underlying grid used for \mathcal{T} has a significant impact on the result. For a same set of parameters, if L designates the maximum length of the domain space Ω measured in pixel/voxel i.e. the resolution of the grid, the characteristic lengths of microstructures are equal to $\frac{\ell_{\parallel}}{L}$ and $\frac{\ell_{\perp}}{L}$. Hence a grid of higher resolution λL will return smaller microstructures by a factor $1/\lambda$, because the characteristics lengths do not vary in pixel/voxel.

643 **Structure thickness.** The thickness of cell edges/filaments can be slightly controlled in the final structure mesh by slightly shifting the isosurface used for the Marching Cube algorithm.

646 7. Results and Applications

647 We present the results of our pattern generation method using PhysOM. All the models are generated on a PC workstation with an Intel Xeon Gold 6148 CPU running at 2.40GHz, 128GB RAM and a GPU Nvidia Quadro RTX6000 with 24 GB memory. Our implementation is based on CuPy library in Python to store the 2D and 3D grids with operations performed in parallel on the GPU. The dimension of the voxel grid and the computational time associated with the full generation of our 3D examples are reported in Table 2. At the exception of Fig. 8, the examples were created from a single grid structure without the per-block optimization. The total time reported corresponds to the simulation for 200 steps. The core of the method relies on uncoupled particle simulation, where each particle update (steps Sense, Rotate, Move, Deposit) is "embarrassingly parallel". The diffusion step and the handling of the 3D texture and its rotation are implemented using trivial and non-optimal

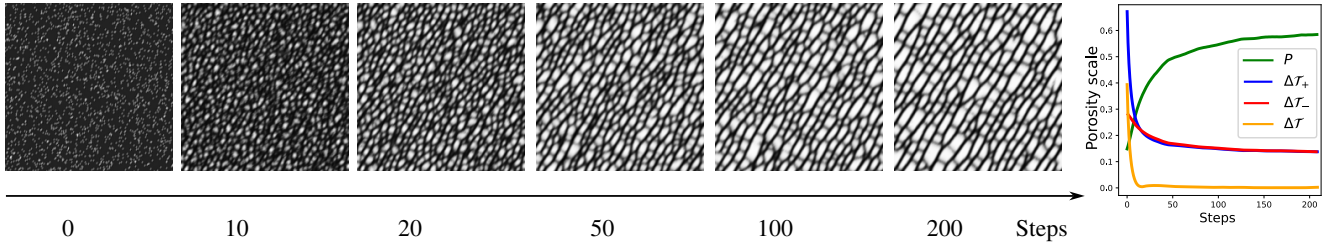


Figure 12: Physarum 2D pattern on a 200×200 grid at several steps on a simulation with the associated curves of porosity P , amount added $\Delta\mathcal{T}_+$, amount removed $\Delta\mathcal{T}_-$ and variation $\Delta\mathcal{T}$. These last three quantities are scaled by a factor that allows them to be visualized on a single plot.

662 algorithms in our case. A very detailed breakdown and fine comparison of timings with other approaches would not be relevant. 663
 664 For instance, [EBPF22] reported measures implemented in C++ with compute shader, while our 3D implementation uses Python. 665
 666 The timings are indeed very different, and our approach could be highly optimized with dedicated developments that are beyond the 667
 668 scope of the current contribution. However, we have developed a real-time 2D prototype relying on WebGL for the entire simulation. 669
 670 This 2D version is obtained as an extension of a standard physarum implementation proposed by Ghassaei [Gha22]. Please refer to the attached video for a visual demonstration of the animated outcomes. 671
 672
 673

	Grid size (voxels)	Total time
Teaser (Fig. 1)	$64 \times 64 \times 768$ (3M)	2 min
Owl (Fig. 3)	$369 \times 306 \times 534$ (60M)	20 min
Eiffel Tow. (Fig. 17a)	$666 \times 247 \times 247$ (40M)	15 min
Chair (Fig. 17b)	$256 \times 256 \times 256$ (16M)	6 min
Femur (Fig. 17c)	$400 \times 210 \times 265$ (22M)	8 min

Table 2: Grid dimension and timings of our 3D examples, for 200 steps of simulation.

674 7.1. Simulation convergence

675 The physarum simulation remains in permanent evolution over the simulation steps which allows a designer to interact with the structure by modifying the grading parameters locally or modifying the trail map by erasing/adding some parts and letting the system adapt at any time. However, for structure generation purposes, we may consider that the system has reached a stable state when the general type of patterns remains consistent over time. We defined this state when the average density of the trail map reaches a stable state. Let us call $\Delta\mathcal{T}_+$ the total amount of density added from Step 3 to Step 4, and $\Delta\mathcal{T}_-$ removed by the decay process from Step 4 to Step 6. We call $\Delta\mathcal{T} = |\Delta\mathcal{T}_+ - \Delta\mathcal{T}_-|$, the net change of density. We consider that the simulation has converged when the relative variation of $\Delta\mathcal{T}/V_\Omega$ remains below a threshold during several steps. The evolution of these parameters along the simulation steps are illustrated in Fig. 12-right. 682
 683
 684
 685
 686
 687
 688
 689

690 7.2. Structural Design for Additive Manufacturing

691 A classical application of microstructure infill is the generation of porous material that can be 3D printed. We show in the following that our approach allows designing materials with varying stiffness and density/porosity in adapting the anisotropy, orientation, and cell area. 692
 693
 694
 695

We introduce the material porosity P , i.e. the reverse of its averaged density, as

$$P = 1 - \frac{1}{V_{\mathcal{T}}} \sum_{\mathbf{x} \in \Omega} \mathcal{T}(\mathbf{x}), \quad (18)$$

698 where $V_{\mathcal{T}}$ is the volume of the infill shape domain $\mathcal{D}_{\mathcal{T}}$. The porosity tends to converge towards a constant value, as depicted in Figure 12-right, also confirming the attainment of a stable state. 699
 700

To confirm the suitability of our generated structure for material design, we propose a study of its anisotropy-dependence deformation using the methodology used in density-based topology optimization [ACS*11]. We apply a continuous vertical compressive stress on generated structure, then simulate and measure the displacement of the global structure using an isotropic linear constitutive stress-strain relation. Each element of the grid $\mathbf{x} \in \Omega$ is associated to a Young's modulus: 701
 702
 703
 704
 705
 706
 707
 708

$$E(\mathbf{x}) = E_{\min} + \mathcal{T}^0(\mathbf{x})(E_0 - E_{\min}). \quad (19)$$

709 Here, E_0 represents the material's stiffness, and E_{\min} is a small stiffness assigned to void regions to prevent the stiffness matrix from becoming singular. \mathcal{T}^0 is the normalized trail in $[0, 1]$. The global stiffness matrix is denoted as $\mathbf{K} = (E(\mathbf{x})\mathbf{k}_0)_{\mathbf{x} \in \Omega}$, where \mathbf{k}_0 corresponds to the stiffness matrix for an element with a unit Young's modulus. The global displacement and force vectors at the grid nodes are represented by \mathbf{U} and \mathbf{F} , respectively. Computing the resulting displacement \mathbf{U} caused by an applied force \mathbf{F} involves solving the equation $\mathbf{K}\mathbf{U} = \mathbf{F}$, which can be expressed as $\mathbf{U} = \mathbf{K}^{-1}\mathbf{F}$. 710
 711
 712
 713
 714
 715
 716
 717

Figure 13-a illustrates the results obtained in applying such constraint while varying the direction and magnitude of the anisotropy. From the isotropic case in the center, we increase the anisotropy, respectively, in the vertical direction on the left-side, and in the horizontal direction on the right-side. This experiment is performed at constant porosity value by selecting tailored values for (ξ, r) . To achieve this, the porosity is computed on small grid samples (200×200) for varying combinations of (ξ, r) , resulting in a density grid representation $P(\xi, r)$. By selecting an iso value of P , the 718
 719
 720
 721
 722
 723
 724
 725
 726

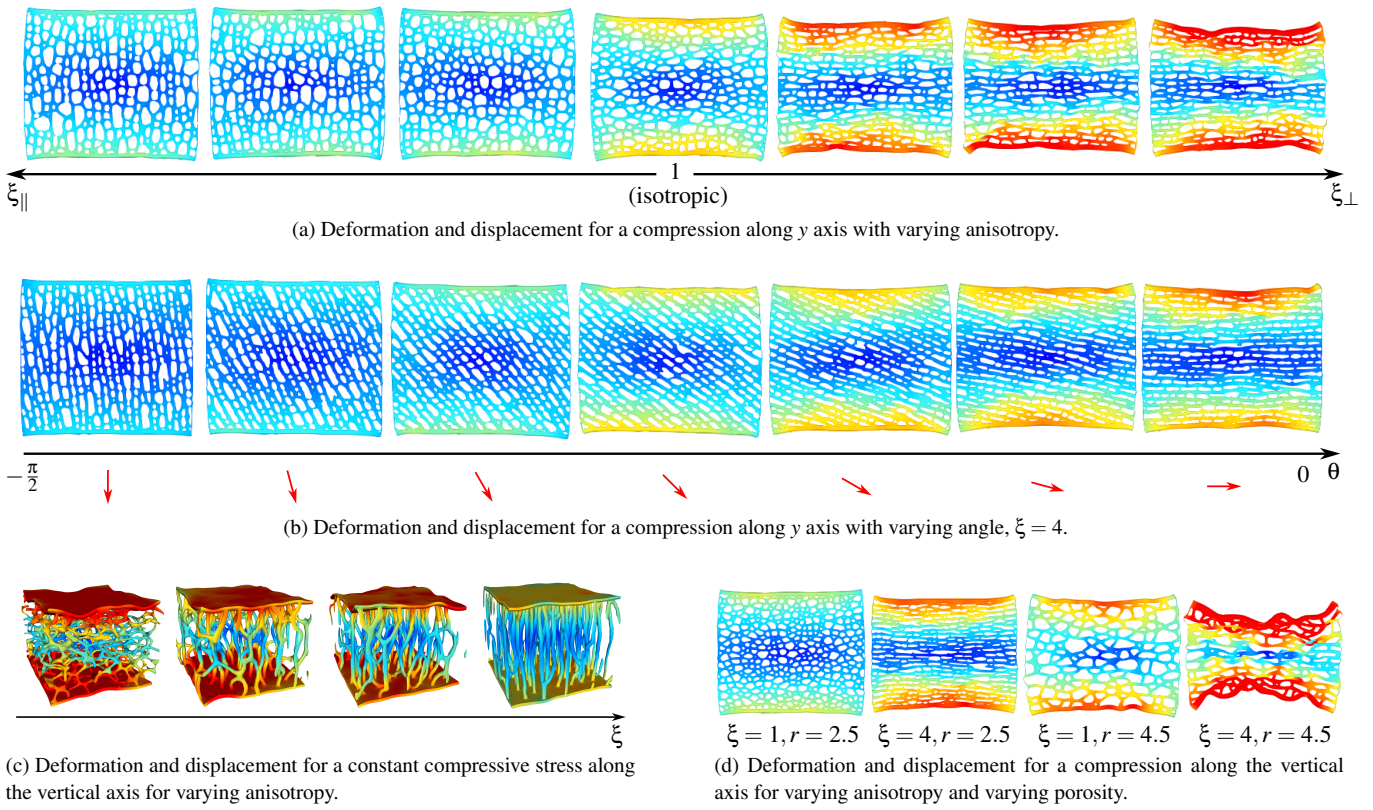


Figure 13: Structural simulations.

727 desired values for (ξ, r) can be obtained. As expected, an increase
 728 of anisotropy in the vertical direction provides stiffer material resistance,
 729 while a horizontal one will lead to a more deformable structure. A similar test is conducted in 3D, as shown in Figure 13-c, using a cubic infill that demonstrates the same property. In Figure 13-b, the anisotropy is held constant while progressively changing the angle from vertical to horizontal, once again reinforcing the same conclusion. Finally, Figure 13-d illustrates the significant influence of material porosity on the resulting displacement. Note that our simulations on 2D quad-meshes and 3D hex-meshes did not consider material nonlinearities, and the large displacement factor in visualization is deliberate. We found these simplifications acceptable for the purpose of validating the effects of the porosity and anisotropy parameters. Indeed, to truly capture such large deformations, a simulation would need to consider geometrical nonlinearities (e.g. buckling), material nonlinearities (e.g. plasticity), as well as internal contacts.

744 Being able to link the parameters of the *Physarum* to the local porosity and anisotropy of the microstructures generated allows for tailored design for deformable shapes. A more in-depth study could allow to map these parameters to material properties or mechanical parameters such as the Young's modulus, similarly to [MSDL17]. More generally, the effective constitutive law for any set of *Physarum* parameters could be evaluated through homoge-

751 nization, thus compiling a reverse mapping from desired mechanical properties to their appropriate generation parameters.

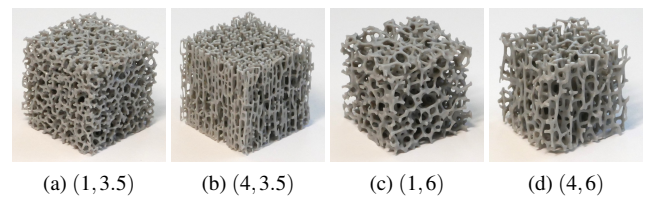
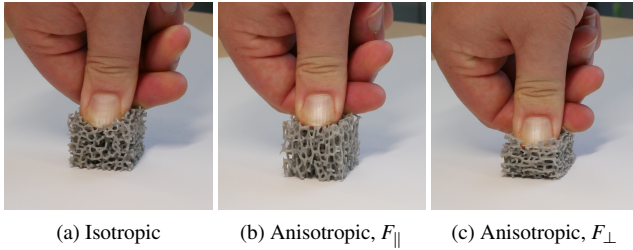


Figure 14: Printed cubic samples with respective varying (ξ, r) values. The numerical models were generated on a $200 \times 200 \times 200$ grid.

753 Based on these observations, our approach is particularly well-suited for printing deformable structures. Figure 14 shows real pictures of printed cubic samples of 3D structures, illustrating both isotropic and anisotropic cases with various r values. These models, along with those showcased in Fig. 17, were generated using the most affordable SLA 3D printer available (Geetech Alkaid) at the time of writing this paper, demonstrating the printability of such structures.

761 Using a flexible material, Fig. 15 demonstrates that the deformation of the structure is highly influenced by its anisotropy and the

763 alignment of the applied force. For a comparable applied pressure,
 764 an anisotropic structure aligned with the force experiences less de-
 765 formation than its isotropic counterpart. Additionally, the isotropic
 766 structure deforms less than the anisotropic structure perpendicular
 767 to the applied force direction, aligning with our numerical simula-
 tions.



(a) Isotropic (b) Anisotropic, F_{\parallel} (c) Anisotropic, F_{\perp}

Figure 15: Pressure applied on cubic samples ($r = 6$) for (a) the isotropic case, (b) the anisotropic case with anisotropy direction aligned with pressure direction, (c) the anisotropic case with anisotropy direction orthogonal to pressure direction.

768

769 In Figure 16, we showcase a comparison of chairs where the top-
 770 left chair is generated from Martinez et al. [MSDL17], designed
 771 using orthotropic k-nearest foams and inspired by the designs of
 772 Lilian van Daal [vD14]. The top-right chair in Figure 16 is obtained
 773 through our PhysOM approach in 2D, employing a similar underly-
 774 ing orientation field. Note that our approach provides aesthetically
 775 pleasing homogeneous organic features and well-defined borders
 776 thanks to the use of the guiding trail \mathcal{T}^* . In Figure 16 (bottom row)
 777 we show pictures of a 3D-printed model with deformation behav-
 778 ior also similar to the one shown in [MSDL17]. These models were
 779 printed using an inexpensive FDM printer (Creality CR-10).

780 7.3. Art and Design

781 Our approach can also find relevant applications in art, design, and
 782 animation. The natural and organic aesthetic of the shapes produced
 783 by PhysOM can be of interest to creative designers and artists. Fig-
 784 ure 17a and 17b showcase our version of the Eiffel Tower and the
 785 biomimicry chair inspired by Lilian van Daal [vD14]. The result-
 786 ing prints are presented Fig. 17e and 17f. It is worth noting that
 787 these structures are dynamic and "alive" as long as the simulation
 788 is running. This characteristic opens up various possibilities, such
 789 as animation or the creation of unique designs. Two structures ex-
 790 tracted from the same simulation but at slightly different time steps
 791 will appear very similar yet distinct, offering opportunities for pro-
 792 ducing diverse and individualized designs.

793 7.4. Biological representation

794 The organic pattern generated by our method can also be desir-
 795 able for representing biological structures. It can be utilized to de-
 796 sign organic textures in 2D, as demonstrated by the dragonfly wing
 797 showcased in Figure 18. Designers can sketch inputs such as the
 798 infill space field or the orientation, specifying labeled areas for
 799 anisotropy. Our method then automatically generates a coherent,

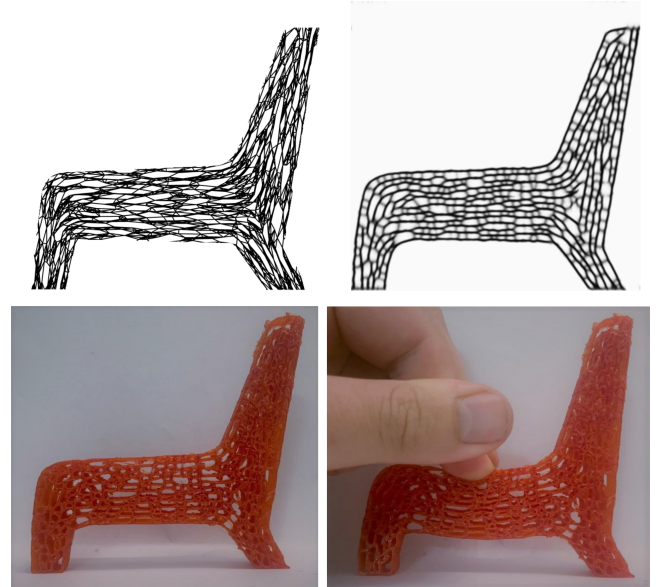


Figure 16: **Top-left:** Chair from Martinez et al. [MSDL17]. **Top-right:** chair designed by PhysOM. **Bottom** Real 3D printed structure. Finger pressure is applied to the chair similarly to [MSDL17].

780

781

782

783

784

785

786

787

788

789

790

791

792

793

794

795

796

797

798

799

800

801

802

803

804

805

806

807

808

809

810

811

812

813

814

815

816

biologically-inspired texture that accurately represents the desired design.

This process can also be applied to 3D application, where, for instance, the patterns formed by *Physarum* organisms bear resemblance to the intricate network of trabeculae found in spongy bones, as illustrated in Figure 17c and Figure 17d.

806 8. Conclusion and Future Work

807 In this work, we have presented a novel approach for generat-
 808 ing intricate organic microstructures inspired by the behavior of
 809 the *Physarum* polycephalum slime mold. By extending the clas-
 810 sical agent-based model of *Physarum* to a 3D domain with lo-
 811 cal anisotropic behavior, we have enabled the design of porous
 812 organic-like microstructures that resemble natural foam-like cells
 813 or filament-like patterns with variable local properties. Our method
 814 offers precise control over the local orientation of 3D patterns, re-
 815 lative cell extension and size (in 2D), and precise infill of 3D forms,
 816 all with well-defined boundaries.

817 The versatility and efficiency of our method make it suitable
 818 for a wide range of applications, including additive manufacturing,
 819 design, and biological representation and engineering. These mi-
 820 crostructures, with their locally stiff or elastic, lighter, and porous
 821 properties, provide interesting mechanical characteristics that can
 822 be adjusted by varying the type of infill patterns. By leveraging
 823 the local rules and time-evolving processes inherent in biological
 824 systems, we have achieved locally adaptable behaviors that give
 825 rise to global emerging structures. This approach allows the end
 826 user to retain control over the evolution of the structure, ensuring
 827 a controllable and visually appealing organic-looking disorder that
 828 enhances strength. This visually appealing appearance of these mi-



Figure 17: Examples of PhysOM model (first line), with their associated prints (second line).

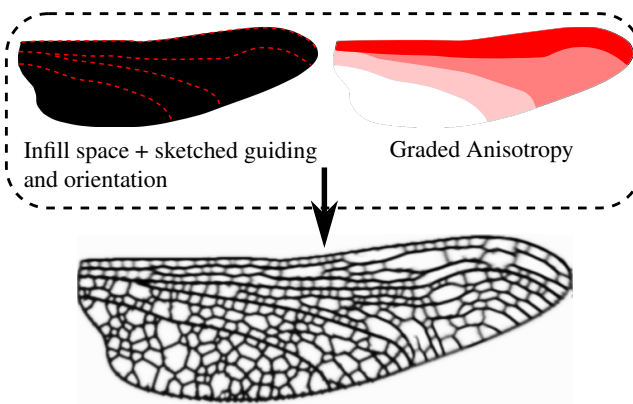


Figure 18: Synthesis of a Dragonfly wing patterns using our approach.

837 tures using the Physarum polycephalum-inspired model shows
 838 promising results, there are certain limitations that should be ac-
 839 knowledged. Firstly, the current implementation focuses on infill-
 840 ing 3D domains with local anisotropic behavior, but it does not
 841 take into account external constraints or specific material proper-
 842 ties. Future work could explore the integration of mechanical and
 843 material considerations to optimize the microstructures for specific
 844 applications. Additionally, the computational costs associated with
 845 simulating large-scale volumes and complex shapes could be a lim-
 846 itation, especially when real-time interactivity is desired. Develop-
 847 ing more efficient algorithms or exploring parallel computing tech-
 848 niques could help address this issue. Furthermore, while our ap-
 849 proach provides control over the evolving structure, there is still
 850 room for improvement in terms of providing intuitive and user-
 851 friendly design interfaces. Future research could investigate inter-
 852 active design tools that enable users to manipulate and guide the
 853 evolution of the microstructures more effectively.

854

829 crostructures, mimicking complex organic materials, offer potential
 830 for art-based design. We believe that our approach will inspire and
 831 assist designers across diverse domains in their pursuit of creating
 832 more complex and visually appealing shapes. Future research direc-
 833 tions may involve exploring additional biological systems and
 834 further refining the control mechanisms to enhance the capabilities
 835 and versatility of our method.

836 While our approach for generating intricate organic microstruc-

855 Conflict of Interest

856 None of the authors have a conflict of interest to disclose.

857 Data Availability

858 Data sharing not applicable to this article as no datasets were gen-
 859 erated or analysed during the current study.

References

- [AAD98] ALEXANDER P., ALLEN S., DUTTA D.: Part orientation and build cost determination in layered manufacturing. *Computer-Aided Design* 30, 5 (1998), 343–356. 2
- [AALS17] AAGE N., ANDREASSEN E., LAZAROV B. S., SIGMUND O.: Giga-voxel computational morphogenesis for structural design. *Nature* 550, 7674 (2017), 84–86. 2
- [ACS*11] ANDREASSEN E., CLAUSEN A., SCHEVENELS M., LAZAROV B. S., SIGMUND O.: Efficient topology optimization in matlab using 88 lines of code. *Structural and Multidisciplinary Optimization* 43, 1 (2011), 1–16. doi:<https://doi.org/10.1007/s00158-010-0594-7>. 12
- [Ada13] ADAMATZKY A.: Physarum wires: Self-growing self-repairing smart wires made from slime mould. *Biomedical Engineering Letters* 3 (2013), 232–241. 3
- [AGDP19] ALLAIRE G., GEOFFROY-DONDERS P., PANTZ O.: Topology optimization of modulated and oriented periodic microstructures by the homogenization method. *Computers & Mathematics with Applications* 78, 7 (2019), 2197–2229. doi:<https://doi.org/10.1016/j.camwa.2018.08.007>. 2
- [Bar09] BARNETT H.: The physarum experiments, 2009. Accessed May 7, 2023. URL: <https://heatherbarnett.co.uk/work/the-physarum-experiments/>. 3
- [BET*20] BURCHETT J. N., ELEK O., TEJOS N., PROCHASKA J. X., TRIPP T. M., BORDOLOI R., FORBES A. G.: Revealing the dark threads of the cosmic web. *The Astrophysical Journal Letters* 891, 2 (2020), L35. 3
- [BL15] BEEKMAN M., LATTY T.: Brainless but multi-headed: decision making by the acellular slime mould physarum polycephalum. *Journal of molecular biology* 427, 23 (2015), 3734–3743. 3
- [BS03] BENDSOE M. P., SIGMUND O.: *Topology optimization: theory, methods, and applications*. Springer Science & Business Media, 2003. 2
- [CHK*05] CHATURVEDI R., HUANG C., KAZMIERCZAK B., SCHNEIDER T., IZAGUIRRE J. A., GLIMM T., HENTSCHEL H. G. E., GLAZIER J., NEWMAN S., ALBER M.: On multiscale approaches to three-dimensional modelling of morphogenesis. *Journal of the Royal Society interface* 2, 3 (2005), 237–253. doi:<https://doi.org/10.1098/rsif.2005.0033>. 3
- [DMM18] DINIZ N., MARIZZI C., MELENDEZ F.: Playing with growth patterns: Merging biotechnology and architectural design to sense environmental toxins. In *Proceedings for 2018 ACSA Fall Conference "PLAY with the rules" 11 – 13 Oct 2018, University of Wisconsin-Milwaukee, Milwaukee US* (2018). 3
- [DPBY*19] DU PLESSIS A., BROECKHOVEN C., YADROITSAVA I., YADROITSEV I., HANDS C. H., KUNJU R., BHATE D.: Beautiful and functional: a review of biomimetic design in additive manufacturing. *Additive Manufacturing* 27 (2019), 408–427. doi:<https://doi.org/10.1016/j.addma.2019.03.033>. 3
- [EBPF20a] ELEK O., BURCHETT J. N., PROCHASKA J. X., FORBES A. G.: Monte carlo physarum machine: An agent-based model for reconstructing complex 3d transport networks. In *Artificial Life Conference Proceedings* 32 (2020), MIT Press One Rogers Street, Cambridge, MA 02142-1209, USA journals-info, pp. 263–265. 2, 3, 6
- [EBPF20b] ELEK O., BURCHETT J. N., PROCHASKA J. X., FORBES A. G.: Polyphorm: Structural analysis of cosmological datasets via interactive physarum polycephalum visualization. *IEEE Transactions on Visualization and Computer Graphics* 27, 2 (2020), 806–816. 3
- [EBPF22] ELEK O., BURCHETT J. N., PROCHASKA J. X., FORBES A. G.: Monte carlo physarum machine: Characteristics of pattern formation in continuous stochastic transport networks. *Artificial Life* 28, 1 (2022), 22–57. 2, 3, 12
- [EHE22] EHRLICH D., HAKIMSHAFI M., ELEK O.: Scaffolding generation using a 3d physarum polycephalum simulation. In *Proceedings of the 7th Annual ACM Symposium on Computational Fabrication* (2022), pp. 1–2. 3
- [Ehr21] EHRLICH D.: Printing the polyphorm: Using 3d printing to manufacture biologically inspired rhizomatic structures. *Thesis, Univ. California Santa Cruz* (2021). 3
- [FW07] FRATZL P., WEINKAMER R.: Nature’s hierarchical materials. *Progress in materials Science* 52, 8 (2007), 1263–1334. doi:<https://doi.org/10.1016/j.pmatsci.2007.06.001>. 3
- [GDAP20] GEOFFROY-DONDERS P., ALLAIRE G., PANTZ O.: 3-d topology optimization of modulated and oriented periodic microstructures by the homogenization method. *Journal of Computational Physics* 401 (2020), 108994. doi:<https://doi.org/10.1016/j.jcp.2019.108994>. 2
- [Gha22] GHASSAEI A.: Physarum transport network, 2022. URL: <https://github.com/amandaghassaei/gpu-io>. 12
- [GKW*19] GARNER E., KOLKEN H. M., WANG C. C., ZADPOOR A. A., WU J.: Compatibility in microstructural optimization for additive manufacturing. *Additive Manufacturing* 26 (2019), 65–75. 2
- [GSR22] GARNIER D.-H., SCHMIDT M.-P., ROHMER D.: Growth of oriented orthotropic structures with reaction/diffusion. *Structural and Multidisciplinary Optimization* 65, 11 (2022), 327. 2
- [How31] HOWARD F. L.: The life history of physarum polycephalum. *American journal of botany* (1931), 116–133. 2, 3
- [Jon09] JONES J.: Approximating the behaviours of physarum polycephalum for the construction and minimisation of synthetic transport networks. In *Unconventional Computation: 8th International Conference, UC 2009, Ponta Delgada, Portugal, September 7-11, 2009. Proceedings* 8 (2009), Springer, pp. 191–208. 2, 3
- [Jon10] JONES J.: Characteristics of pattern formation and evolution in approximations of physarum transport networks. *Artificial life* 16, 2 (2010), 127–153. 2, 3, 4, 7, 11
- [Jon15] JONES J.: *From pattern formation to material computation: multi-agent modelling of Physarum Polycephalum*, vol. 15. Springer, 2015. 2, 3, 4, 5, 6
- [KTZK20] KUMAR S., TAN S., ZHENG L., KOCHMANN D. M.: Inverse-designed spinodoid metamaterials. *npj Computational Materials* 6, 1 (2020), 73. 2
- [Lak93] LAKES R.: Materials with structural hierarchy. *Nature* 361, 6412 (1993), 511–515. doi:<https://doi.org/10.1038/361511a0>. 3
- [LCL*21] LIU B., CHENG H., LIU M., CAO W., JIANG K.: Adaptive anisotropic porous structure design and modeling for 2.5 d mechanical parts. *Materials & Design* 206 (2021), 109786. 2
- [LS03] LABELLE F., SHEWCHUK J. R.: Anisotropic voronoi diagrams and guaranteed-quality anisotropic mesh generation. In *Proceedings of the nineteenth annual symposium on Computational geometry* (2003), pp. 191–200. 2
- [MDL16] MARTÍNEZ J., DUMAS J., LEFEBVRE S.: Procedural voronoi foams for additive manufacturing. *ACM Transactions on Graphics (TOG)* 35, 4 (2016), 1–12. 2
- [MHSL18] MARTÍNEZ J., HORNUS S., SONG H., LEFEBVRE S.: Polyhedral voronoi diagrams for additive manufacturing. *ACM Transactions on Graphics (TOG)* 37, 4 (2018), 1–15. 2
- [MSDL17] MARTÍNEZ J., SONG H., DUMAS J., LEFEBVRE S.: Orthotropic k-nearest foams for additive manufacturing. *ACM Transactions on Graphics (TOG)* 36, 4 (2017), 1–12. 1, 2, 13, 14
- [MX17] MA Y., XU W.: Physarealm—a bio-inspired stigmergic algorithm tool for form-finding. In *Protocols, Flows and Glitches, Proc. 22nd Int. Conf. Association for Computer-Aided Architectural Design Research in Asia (CAADRIA) 2017* (2017), pp. 499–509. 3, 5, 6
- [Nak01] NAKAGAKI T.: Smart behavior of true slime mold in a labyrinth. *Research in Microbiology* 152, 9 (2001), 767–770. 3

- 986 [NVSA17] NTINAS V., VOURKAS I., SIRAKOULIS G. C.,
987 ADAMATZKY A. I.: Oscillation-based slime mould electronic cir-
988 cuit model for maze-solving computations. *IEEE Transactions on*
989 *Circuits and Systems I: Regular Papers* 64, 6 (2017), 1552–1563. 3
- 990 [NYT00] NAKAGAKI T., YAMADA H., TÓTH Á.: Maze-solving by an
991 amoeboid organism. *Nature* 407, 6803 (2000), 470–470. 3
- 992 [NYT01] NAKAGAKI T., YAMADA H., TOTH A.: Path finding by tube
993 morphogenesis in an amoeboid organism. *Biophysical chemistry* 92, 1-2
994 (2001), 47–52. 3
- 995 [PMNWW19] PODROUŽEK J., MARCON M., NINČEVIĆ K., WAN-
996 WENDNER R.: Bio-inspired 3d infill patterns for additive manufacturing
997 and structural applications. *Materials* 12, 3 (2019), 499. doi:<https://doi.org/10.3390/ma12030499>. 3
- 998
999 [PT08] PANTZ O., TRABELSI K.: A post-treatment of the homogeniza-
1000 tion method for shape optimization. *SIAM Journal on Control and Op-*
1001 *timization* 47, 3 (2008), 1380–1398. doi:[https://doi.org/10.](https://doi.org/10.1137/070688900.2)
1002 [1137/070688900.2](https://doi.org/10.1137/070688900.2)
- 1003 [PVK*20] PORTELA C. M., VIDYASAGAR A., KRÖDEL S., WEIS-
1004 SENBACH T., YEE D. W., GREER J. R., KOCHMANN D. M.: Ex-
1005 treme mechanical resilience of self-assembled nanolabyrinthine materi-
1006 als. *Proceedings of the National Academy of Sciences* 117, 11 (2020),
1007 5686–5693. 2
- 1008 [PZM*15] PANETTA J., ZHOU Q., MALOMO L., PIETRONI N.,
1009 CIGNONI P., ZORIN D.: Elastic textures for additive fabrication. *ACM*
1010 *Transactions on Graphics (TOG)* 34, 4 (2015), 1–12. 2
- 1011 [Que20] QUEFFURUS O.: Phys [art] um: pour une approche artistique de
1012 la culture de physarum polycephalum. 3
- 1013 [RB13] REID C. R., BEEKMAN M.: Solving the towers of hanoi—how an
1014 amoeboid organism efficiently constructs transport networks. *Journal of*
1015 *Experimental Biology* 216, 9 (2013), 1546–1551. 3
- 1016 [RLDB12] REID C. R., LATTY T., DUSSUTOUR A., BEEKMAN M.:
1017 Slime mold uses an externalized spatial “memory” to navigate in com-
1018 plex environments. *Proceedings of the National Academy of Sciences*
1019 *109*, 43 (2012), 17490–17494. 3
- 1020 [Sch13] SCHUBERT T.: Bodymetries, 2013. Accessed May 7,
1021 2023. URL: [https://www.theresaschubert.com/works/](https://www.theresaschubert.com/works/bodymetries/)
1022 [bodymetries/](https://www.theresaschubert.com/works/bodymetries/). 3
- 1023 [Seb23] SEBDON M.: Crtl, 2023. Accessed May 7, 2023. URL: <https://michaelsebdon.com/C-t-r-l>. 3
- 1024
1025 [Sig95] SIGMUND O.: Tailoring materials with prescribed elastic proper-
1026 ties. *Mechanics of materials* 20, 4 (1995), 351–368. 2
- 1027 [SPG19] SCHMIDT M.-P., PEDERSEN C. B., GOUT C.: On structural
1028 topology optimization using graded porosity control. *Structural and*
1029 *Multidisciplinary Optimization* 60, 4 (2019), 1437–1453. doi:<https://doi.org/10.1007/s00158-019-02275-x.2>
- 1030
1031 [TKN07] TERO A., KOBAYASHI R., NAKAGAKI T.: A mathematical
1032 model for adaptive transport network in path finding by true slime mold.
1033 *Journal of theoretical biology* 244, 4 (2007), 553–564. 3
- 1034 [TNT*10] TERO A., NAKAGAKI T., TOYABE K., YUMIKI K.,
1035 KOBAYASHI R.: A method inspired by physarum for solving the
1036 steiner problem. *International journal of unconventional Computing* 6,
1037 2 (2010). 3
- 1038 [TS12] TSOMPANAS M.-A. I., SIRAKOULIS G. C.: Modeling and hard-
1039 ware implementation of an amoeba-like cellular automaton. *Bioinspira-*
1040 *tion & Biomimetics* 7, 3 (2012), 036013. 3
- 1041 [TTS*10] TERO A., TAKAGI S., SAIGUSA T., ITO K., BEBBER D. P.,
1042 FRICKER M. D., YUMIKI K., KOBAYASHI R., NAKAGAKI T.: Rules
1043 for biologically inspired adaptive network design. *Science* 327, 5964
1044 (2010), 439–442. 3
- 1045 [TTZ*20] TRICARD T., TAVERNIER V., ZANNI C., MARTÍNEZ J.,
1046 HUGRON P.-A., NEYRET F., LEFEBVRE S.: Freely orientable mi-
1047 crostructures for designing deformable 3d prints. *ACM Trans. Graph.*
1048 *39*, 6 (2020), 211–1. 2
- [vD14] VAN DAAL L.: Biomimicry; 3d printed soft seat, 2014. Ac-
cessed June 8, 2023. URL: [https://www.lilianvandaal.com/](https://www.lilianvandaal.com/biomimicry-3d-printed-soft-seat)
[biomimicry-3d-printed-soft-seat](https://www.lilianvandaal.com/biomimicry-3d-printed-soft-seat). 14
- [vEYC*21] VAN EGMOND D. A., YU B., CHOUKIR S., FU S., SINGH
C. V., HIBBARD G., HATTON B. D., ET AL.: The benefits of struc-
tural disorder in natural cellular solids. *arXiv preprint arXiv:2110.04607*
(2021). 2
- [WAWS18] WU J., AAGE N., WESTERMANN R., SIGMUND O.: Infill
optimization for additive manufacturing—approaching bone-like porous
structures. *IEEE Transactions on Visualization and Computer Graph-*
ics 24, 2 (2018), 1127–1140. doi:[https://doi.org/10.1109/](https://doi.org/10.1109/TVCG.2017.2655523.2)
[TVCG.2017.2655523.2](https://doi.org/10.1109/TVCG.2017.2655523.2)
- [WSG21] WU J., SIGMUND O., GROEN J. P.: Topology optimization
of multi-scale structures: A review. *Structural and Multidisciplinary*
Optimization 63 (2021), 1455–1480. doi:[https://doi.org/10.](https://doi.org/10.1007/s00158-021-02881-8.2)
[1007/s00158-021-02881-8.2](https://doi.org/10.1007/s00158-021-02881-8.2)
- [WWG21] WU J., WANG W., GAO X.: Design and optimization of con-
forming lattice structures. *IEEE transactions on visualization and com-*
puter graphics 27, 1 (2021), 43–56. doi:[https://doi.org/10.](https://doi.org/10.1109/TVCG.2019.2938946.1)
[1109/TVCG.2019.2938946.1](https://doi.org/10.1109/TVCG.2019.2938946.1)
- [WWZW16] WU J., WANG C. C., ZHANG X., WESTERMANN R.:
Self-supporting rhombic infill structures for additive manufacturing.
Computer-Aided Design 80 (2016), 32–42. 2
- [ZSCM17] ZHU B., SKOURAS M., CHEN D., MATUSIK W.: Two-
scale topology optimization with microstructures. *ACM Transactions*
on Graphics (TOG) 36, 4 (2017), 1. 2
- [ZWZ*20] ZHANG Y., WANG Z., ZHANG Y., GOMES S., BERNARD
A.: Bio-inspired generative design for support structure generation
and optimization in additive manufacturing (am). *CIRP Annals* 69, 1
(2020), 117–120. doi:[https://doi.org/10.1016/j.cirp.](https://doi.org/10.1016/j.cirp.2020.04.091.3)
[2020.04.091.3](https://doi.org/10.1016/j.cirp.2020.04.091.3)
- [ZZD11] ZHANG Y. J., ZHANG Z. L., DENG Y.: An improved maze
solving algorithm based on an amoeboid organism. In *2011 Chinese*
Control and Decision Conference (CCDC) (2011), IEEE, pp. 1440–
1443. 3